Ultrasensitive All-Optical Thermometry Using Nanodiamonds with a High Concentration of Silicon-Vacancy Centers and Multiparametric Data Analysis

Sumin Choi,[†] Viatcheslav N. Agafonov,[‡] Valery A. Davydov,[§] and Taras Plakhotnik[*,†]

[†]School of Mathematics and Physics, The University of Queensland, QLD 4072, Australia
[‡]GREMAN, UMR CNRS-7437, University F. Rabelais, 37200 Tours, France
[§]L.F. Vereshchagin Institute for High Pressure Physics, The Russian Academy of Sciences, Troitsk, Moscow 108840, Russia

S Supporting Information

ABSTRACT: Nanoscale thermometry is paramount to study primary processes of heat transfer in solids and is a subject of hot debate in cell biology. Here we report ultrafast temperature sensing using all-optical thermometry, exploiting synthetic nanodiamonds with silicon-vacancy (SiV) centers embedded at a high concentration. Using multiparametric analysis of photoluminescence (PL) of these centers, we have experimentally achieved an intrinsic noise floor of about 13 mK Hz$^{-1/2}$, which is a 1000-fold increase in the readout speed in comparison to the current record values demonstrated with all-optical methods of comparable spatial-resolution and precision. Our thermometers are smaller than 250 nm across but can detect a 0.4 °C change of temperature in a measurement taking only 0.001 s. The exceptional sensitivity and simplicity of these thermometers enable a wide range of applications such as temperature monitoring and mapping within intracellular regions and in state-of-the-art solid-state electronic nanodevices.

KEYWORDS: *nanodiamond, all-optical thermometry, color centers, silicon vacancy center*
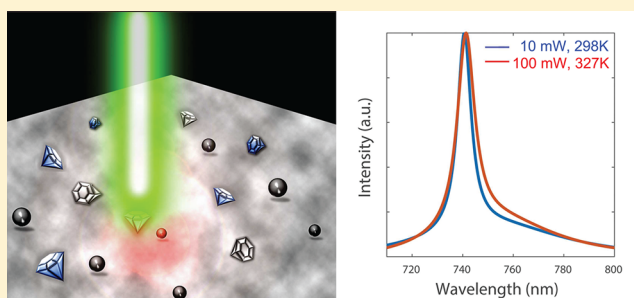
There is a high demand for the development of ultrasmall, noninvasive, fast, and reliable nanothermometry for temperature monitoring intracellularly in vitro and in small organisms.[1−3] Heat produced by living species has been known for centuries but viewed merely as a factor contributing to body temperature. Recent progress in ultralocal thermometry down to subcellular spatial resolution has challenged this concept, but the accuracy of such measurements has been questioned. While several different types of optical nano-thermometers are being developed using quantum dots,[4] organic dyes,[5] nanostructures,[6] and luminescent proteins,[7] a heated discussion has been sparked about the reliability of temperature measurements in cells and the applicability of theoretical concepts based on scaling laws and macroscopic thermodynamics to the complex intracellular interior.[8−11] Reduced size of solid state devices with faster switching speeds has also increased the need for accurate and fast temperature measurement with submicron resolution, especially during real-time operation.[12] Detection of local temperature is extremely important due to the complexity of the heat transport on the nanoscale where the conventional Fourier's law breaks down.[13] Thus, development of fast nanothermometers free of artifacts is highly crucial.

During past decades a very active field of noninvasive optical nanothermometry has emerged,[14,15] where nanodiamonds imbedded with color centers have attracted much interest[3,16,17] due to their remarkable optical properties,[18] biocompatibility,[19] and uncomplicated surface functionalization.[20] Although a large number of color centers exists in diamond, nitrogen vacancy (NV) combined with optically detected magnetic resonance (ODMR) technique have dominated research.[21−23] The limits in precision are conventionally expressed in terms of a noise floor and have been reported as small as 130 mK Hz$^{-1/2}$ and 25 mK Hz$^{-1/2}$ using single NV centers[16] and a magnetic nanoparticle hybrid nanodiamond,[24] respectively. However, ODMR measurements require microwave radiation that can induce sensitive temperature changes at cellular levels[25] and are quite complicated in implementation. Both factors are undesirable for biological applications.

Alternatively, a simple all-optical method of temperature measurements with NV centers has been demonstrated recently[21] using a feature in their luminescence spectra called a zero phonon line (ZPL). However, the strength of the ZPL in NV centers is very small, and this limits the noise floor to 0.3 K Hz$^{-1/2}$. Other centers with stronger ZPL transitions such as silicon vacancy (SiV),[26] germanium vacancy (GeV),[27] and tin vacancy (SnV)[28] have emerged as promising candidates for

temperature sensing, but their reported precisions are similar to the value obtained with NV centers: 0.5 K $Hz^{-1/2}$ (SiV in 200 nm crystal) and 0.3 K $Hz^{-1/2}$ (GeV^{27} and SnV^{28} in a bulk crystal).

Here we show ultrasensitive all-optical temperature measurements using photoluminescence (PL) of SiV centers in diamonds smaller than 250 nm and demonstrate an intrinsic noise floor of about 13 mK $Hz^{-1/2}$, a dramatic improvement of the current record values. This reduction of the noise is equivalent to a 1000-fold decrease of the acquisition time for a given precision of thermometry. The factor of 1000 has two contributions. A part on the order of 100 is due to the improvement in the crystal growth process that allows for a much higher concentration of SiV; the remaining order of magnitude is obtained by developing a novel method of data analysis.

■ RESULTS AND DISCUSSION

Details of optical measurements are presented in Experimental Section. An example of a spectrum is shown in Figure 1a.
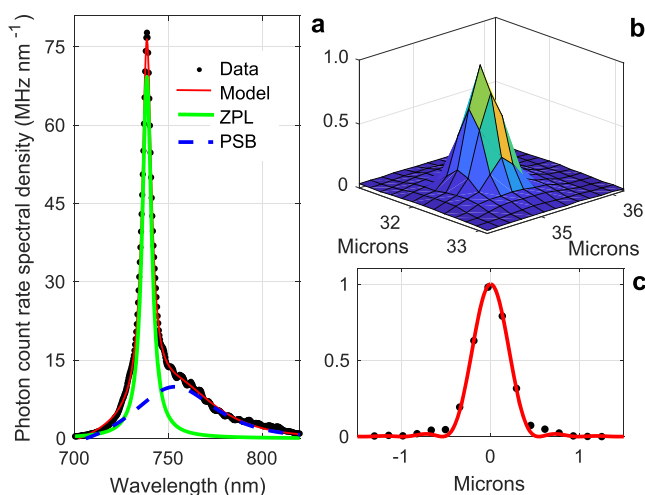
Figure 1. (a) PL spectrum of a diamond crystal with SiV centers. Black dots show experimental data. At 50 mW laser power (0.55 MW cm^{-2} power density at the location of the crystal) the detected photon count rate is about 0.8 GHz. The red curve is the best fit of the function defined by eq 1 to the experimental data. The green and blue curves show the ZPL and the PSB, respectively. Panel (b) shows an optical image of a typical bright crystal with vertical scale proportional to the luminescence intensity. Panel (c) shows a cross-section of the image in (b) scaled vertically and shifted horizontally to overlap with a theoretical point spread function (red line) of the microscope objective.

Luminescence spectra of the SiV center can be split into two distinctive bands, a strong ZPL at around 740 nm and the phonon sideband (PSB), an approximately 25 nm broad feature to the right of the ZPL. We did not observe significant spectral signatures of other defect centers in the measured nanodiamonds. This is important because the presence of different color centers with overlapping spectra[29] results in the complexity of the data analysis. In the present case, SiV spectra are accurately modeled with the function $\Phi(\lambda)$ below, a sum of two Lorentzians and background $B(\lambda) = b_0 + b_1\lambda$ (assumed to be a straight line representing a possible contribution from the substrate) multiplied by an overall scaling factor R_0.

$$\Phi(\lambda) = R_0 \left[A_{zpl} \frac{\gamma^2}{4(\lambda - \lambda_{zpl})^2 + \gamma^2} + \frac{\Gamma^2}{4(\lambda - \lambda_{psb})^2 + \Gamma^2} + B(\lambda) \right]$$

(1)

Generally, the temperature of the crystal affects the widths of the ZPL and of the PSB (γ and Γ, respectively), the peak positions of each Lorentzian (λ_{zpl} and λ_{psb}), and the relative amplitude of the ZPL (A_{zpl}). Some of the parameters appear to be more sensitive than others. These dependencies are used for temperature sensing.

Figure 1b shows a typical optical image of a crystal, direct evidence that the data are collected from a small object. A vertical cross-section of the image in Figure 1b is shown in Figure 1c, together with a diffraction limited point spread function (PSF) for a microscope objective with NA = 0.9 and at the wavelength of 740 nm (all as in the experiment). The agreement between the experimental data and the theoretical PSF indicates that the size of the light emitting object is not larger than 250 nm.

The most probable values of γ, Γ, λ_{zpl}, λ_{psb}, and A_{zpl} have been found from experimental spectra using conventional least-squares fitting. It is important to note that, although this method has theoretical justifications (a normal distribution of the errors in the intensity at every spectral point and statistical independences of these errors), such a routinely used "fitting" may result in unphysical correlations between the fitted parameters. For example, fitting a single Lorentzian to a spectrum creates a correlation between the peak value of the Lorentzian and its width[30] (see the reference and Supporting Information for other examples). Such correlations are not caused by mutual physical dependence of the fitted parameters, but results from the dependence of the minimal value of χ^2-function (the criteria for the best fitting) on these parameters. These correlations are important and will be discussed in relation to temperature measurements.

A series of SiV-spectra has been measured at different excitation laser powers. The resulting values of γ and A_{zpl} versus λ_{zpl} are plotted in Figure 2. It can be seen that the
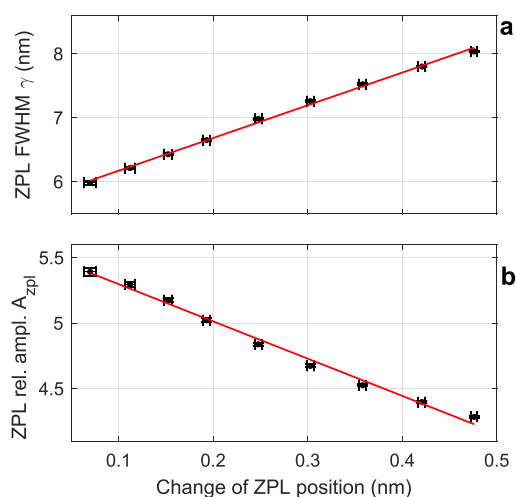
Figure 2. Values of (a) γ and (b) A_{zpl} vs the change of λ_{zpl}. The gradients of the red lines are 5.1 ± 0.2 and -2.8 ± 0.2 nm^{-1}, respectively. The change of λ_{zpl} is shown relative to the value obtained by extrapolating λ_{zpl} to zero laser power (in this case, the temperature of the crystals equals 21 °C, the lab temperature). In the shown range of data, the temperature varies approximately from 25 to 54 °C.
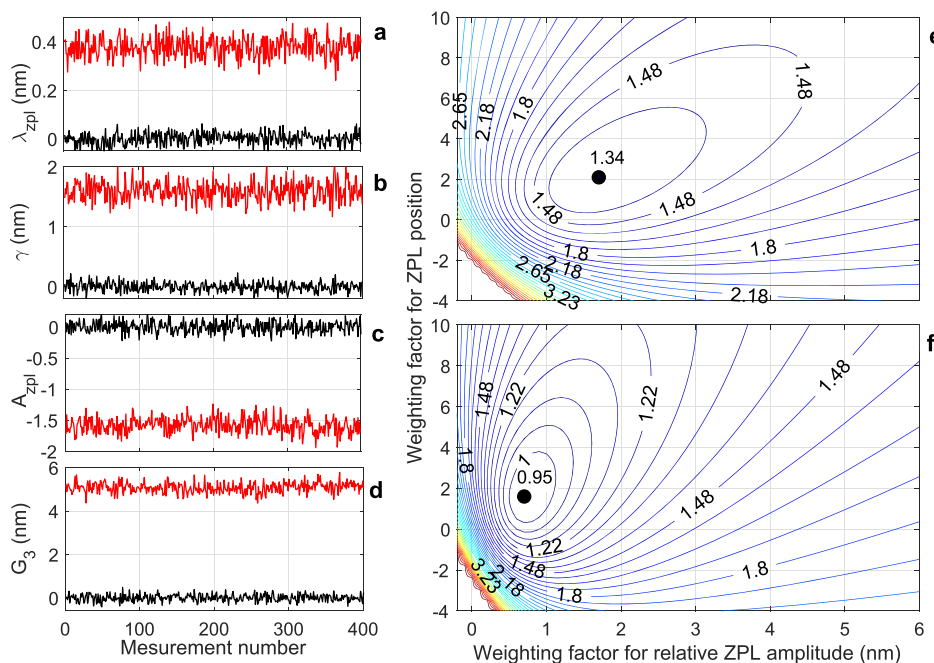
Figure 3. Multiparametric data analysis at the measurement time of 0.1 ms. On the left: Temperature sensing using a single parameter. The black lines are recorded at laser power of 6 mW (estimated temperature 298 K) and the red lines are recorded at 50 mW ($T \approx 327$ K). All curves are shifted vertically so that the average values at the lower temperature are zero. (a) ZPL peak position λ_{zpl}, (b) ZPL width γ, (c) ZPL relative amplitude A_{zpl}, and (d) G_3 with weighting factors optimized for the best precision. On the right: The contour plots show σ_T in units of K as a function of w_λ and w_A. Panel (e) is the standard deviation calculated using 50 mW data and (f) obtained using spectra simulated with experimental parameters substituted into eq 1 and added Poisson noise. The black dots locate the weighting factors for the best precision of the temperature.

broadening of the ZPL is about 5× larger than the corresponding shift. A similar trend has been reported for dependence of the ZPL on temperature.[31] We believe that this heating is related to a high concentration of silicon in the primary mixture for crystal growth (see Experimental Section). The excess of silicon forms approximately spherical objects, which are mixed with nanodiamonds in the final product (see Supporting Information). Silicon spheres (some of them partially oxidized) can be dissolved and removed from the product but here they were used for heating. The absorption of light by these impurities increases the temperature of nearby diamonds and, thus, their thermal properties can be investigated without the need of an external heating element. The temperature could be simply varied by changing the power density of the exciting laser light at the location of the spheres. The laser-induced heating is most significant when the microscope objective operates in a wide field excitation mode. In a confocal mode when the laser light is tightly focused, this heating is reduced by an order of magnitude for the same power density at the location of the diamond crystal (see Supporting Information). This proves that the heating is not caused by absorption of light in the diamond crystal itself.

The temperature change of a specific diamond crystal can be accessed using one of the parameters defining the luminescence spectrum of SiV. We have used the peak wavelength of the ZPL which has been studied several times and for which a value of its temperature sensitivity $s_{\lambda_{zpl}} \equiv d\lambda_{zpl}/dT \approx 0.012$ nm K^{-1} has been reported.[26,32] Variation of properties is common for nanoparticles (see Table S1 of the Supporting Information) and calibration of each crystal is required for measurements where the accuracy of better than 20% is essential. Temperature sensitivity of all other parameters could be obtained using the sensitivity of the λ_{zpl} as a reference. For example, sensitivity

of the ZPL width and its relative amplitude can be estimated as about $s_\gamma = 0.062$ nm K^{-1} and $s_A = 0.037$ K^{-1}, respectively, using the data shown in Figure 2.

Due to the correlation mentioned above, even temperature-independent parameters may unfavorably affect the precision of the temperature estimate by transferring their noise to temperature-dependent parameters. The multiparametric analysis eliminates the effect of correlation to achieve the best outcome from the measurements. A general approach is described in the Experimental Section. In this case, we have used the following linear combination of three parameters as a single temperature sensing factor
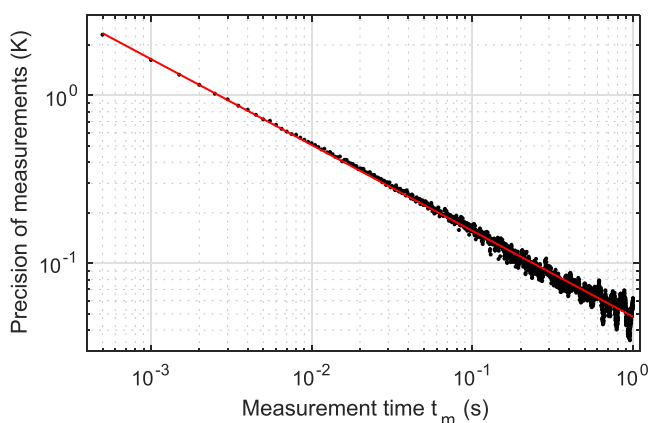
$$G_3 = \gamma + w_\lambda \lambda_{zpl} - w_A A_{zpl} \qquad (2)$$

Addition of other parameters to the linear combination has insignificantly improved the results. The procedure of finding the optimal values of the weighting factors is outlined below.

Panels a−c in Figure 3 show λ_{zpl}, γ, and A_{zpl} determined for two sets of 400 spectra each recorded with 0.1 ms integration time at two temperatures. It is important to emphasize that we simultaneously measure the complete spectrum of SiV using a CCD. Fluctuations of the laser power do not affect ZPL width, ZPL position, and the relative amplitude of the ZPL; only the overall scaling factor is affected. The best precision was determined at the higher temperature (also, higher laser power), while data at the lower temperature have been used for thermal sensitivity calibration. The optimal values of $w_\lambda \approx 2.1$ and $w_A \approx 1.7$ nm (note that factor w_A has units, while w_λ is dimensionless) were determined empirically, as shown in Figure 3e,f by plotting the values of σ_T versus w_λ and w_A. The three-parametric sensing method improves the precision, as can be seen in Figure 3d. Given the measuring (integration) time $t_m = 0.1$ ms, the minimal standard deviation of 1.34 ± 0.1

K corresponds to the noise floor $\eta_T \equiv \sigma_T t_m^{1/2} = 13.4 \pm 1$ mK Hz$^{-1/2}$. A single-parameter (ZPL width) case corresponds to the point with coordinates $w_\lambda = 0$ and $w_A = 0$ in Figure 3e. It can be seen that the multiparametric analysis improves the precision by a factor of approximately 2.5 in this case, in comparison to the results achieved using ZPL width or ZPL peak position alone. Equivalently, it decreases the measurement time by 6-fold if the precision is kept at a fixed value. Monte Carlo simulations of the spectra with Poissonian noise result in the minimal standard deviation of 0.95 K (see Figure 3f). This value is approximately $\sqrt{2}\times$ smaller than the 1.34 K due to the noise excess factor[33] of electron-multiplying CCDs. If the data were taken without electron multiplication (for example, with a sCMOS camera) the noise floor would be reduced to about 10 mK Hz$^{-1/2}$. The precision is inversely proportional to the square-root of the integration time (see below) and, for example, improves to (0.4 ± 0.1) K at 1 ms. Previously, a similar precession with diamond color centers has been obtained[28] only after integration for 1 s. We also investigated other nanodiamonds, and the results are presented in the Supporting Information.

As an ultimate demonstration of our method, we have recorded 20000 spectra with 0.5 ms integration time and power density of the exciting laser reduced to about 70 kW cm^{-2}, a value more common for intracellular studies. This set of data has been used to obtain precision of the temperature measurements at different integration times. For example, one can obtain 100 spectra with effective integration times of 0.1 s and calculate the corresponding standard deviation by splitting the entire data set into 100 subsets and averaging each. Results obtained in this way for integration times up to 1 s are shown in Figure 4 where the highest precision is better than 50 mK. Long integration times undesirably affect λ_{zpl} more than other parameters. The 50 mK change of temperature shifts the ZPL by 6×10^{-4} nm spectrally and by about 30 nm on the CCD sensor. Due to the magnification of the microscope objective, a 1 nm shift of the nanocrystal position displaces ZPL comparably with the thermal shift. For this reason, λ_{zpl} has not been used to obtain the results shown in Figure 4 (see the figure caption).

It is interesting to compare the achieved precision of nanothermometers with the fundamental limit set by thermodynamics on the concept of temperature. Due to the small size, the temperature of a nanodiamond fluctuates and these and these fluctuations can be characterized by a standard deviation σ_{th} expressed as

$$\sigma_{th} = T\sqrt{\frac{k_B}{vc_v}} \tag{3}$$

where k_B is the Boltzman's constant, v is the volume of the crystal, and c_v is the constant volume heat capacity of diamond per unit volume.[34] σ_{th} calculated for a 250 nm sphere of diamond at $T \approx 300$ K is about 10 mK and is close to the precision of our thermometers. The characteristic time scale of these fluctuations (τ_{rel}) is defined by the heat exchange between the crystal and its environment. A nanodiamond immersed in a homogeneous media has τ_{rel} on the order of a^2/α, where a is the radius of the crystal and α is the thermal diffusivity of the media. The observed thermal fluctuations equal $\sigma_{th}(\tau_{rel}/t_m)^{1/2}$, and therefore, the limit on the noise floor set by thermal fluctuations is $\eta_{th,T} = \sigma_{th}(\tau_{rel})^{1/2} \approx T[k_B/(ac_v\alpha)]^{1/2}$. Substitution of the numerical values results in $\eta_{th,T} \approx 6$ μK Hz$^{-1/2}$ for a 250 nm diamond in water at room temperature.

In conclusion, we have obtained 13 mK Hz$^{-1/2}$ noise floor in all-optical thermometry using diamonds smaller than 250 nm doped with SiV centers. Theoretically, the noise floor can be further reduced to about 10 mK Hz$^{-1/2}$ if the noise excess factor of the electron-multiplying CCDs is eliminated. A high SiV concentration and multiparametric analysis enable about 1000× faster measurements if compared to any reported up to date all-optical detection schemes with sub-250 nm spatial resolution. The value for the noise floor is valid for integration times as long as 1 s.

■ EXPERIMENTAL SECTION

Sample Preparation. Nanodiamonds with SiV impurity-vacancy color centers were obtained by high pressure−high temperature (HPHT) treatment of the catalyst metal-free hydrocarbon growth system based on homogeneous mixtures of naphthalene, $C_{10}H_8$ (Chemapol), and tetrakis-(trimethylsilyl)sylane, $C_{12}H_{36}Si_5$ (Stream Chemicals Co.), which were used as the doping component.[35] Cold-pressed tablets of the initial mixture (5 mm diameter and 4 mm height) were placed into a graphite container, which simultaneously served as a heater of the high-pressure toroid-type apparatus. The experimental procedure consisted of loading the high-pressure apparatus to 8.0 GPa at room temperature, heating the sample to the temperature of diamond formation (1400 °C), and short (10 s) isothermal exposure of the sample at this temperature. The obtained high-pressure states have been isolated by quenching to room temperature under pressure and then complete pressure release. The recovered diamond materials have been characterized under ambient conditions by using X-ray diffraction, Raman spectroscopy, and scanning and transmission electron microscopies (SEM and TEM). The nanodiamonds are dispersed with deionized water and treated with 120 W power ultrasound for 30 s. Then the nano-

Figure 4. Precision σ_T of temperature measurement at 6 mW laser power (corresponds to 4 K above the lab temperature) at different measurement times t_m. The laser power density at the location of the nanodiamond and the detected photon rate are approximately 70 kW cm^{-2} and 40 MHz. $G_2 = \gamma - 0.42$ nm $\times A_{zpl}$ is used for thermometry. The straight line corresponds to the theoretical dependence $\sigma_T \propto 1/\sqrt{t_m}$, where the proportionality constant is the noise floor $\eta_T = 49 \pm 1$ mK Hz$^{-1/2}$. It is confirmed by numerical simulations (not shown) that due to the excess noise of the EMCCD, this value is $\sqrt{2}\times$ larger than it should be theoretically for the given count rate and Poisson statistics of the noise.

diamonds are drop-cast on a cover glass for optical characterization. The mean size of nanodiamonds is about 70 nm, but much larger crystals are present in the sample.

Optical Measurements. The optical measurements are made with a home-built confocal microscope at room temperature. Off-resonant excitation light from a continuous-wave 532 nm laser is focused onto the sample through an air objective ×100 and NA = 0.90 (Nikon). The emission passes through a dielectric filter to reject the excitation light, then is collected into an EMCCD (iXon Andor). The apparatus can work in imaging or spectroscopic modes (with Acton 2300i grating spectrometer) and use wide-field or confocal illumination. In the confocal mode, the laser light intensity in the focal spot is proportional to $\exp(-r^2/r_0^2)$, where r is the distance from the center of the spot (and the location of the investigated crystals) and $r_0 = 1.2$ μm. This can be used to estimate the power density of light at the center of the spot to be 11 MW cm^{-2} at 1 W output of the exciting laser (taking into account about 50% loss of power on all optical elements of the experimental setup).

Data Analysis. It is assumed that the probability distribution function for the model parameters is proportional to $\exp\left(-\frac{1}{2}\chi^2(\boldsymbol{Y})\right)$, where $\boldsymbol{Y} \equiv (Y_1, Y_2, ..., Y_M)^T$ is a vector in the parameter space. The χ^2-function in the vicinity of its minimum can be approximated by Taylor series

$$\chi^2(\boldsymbol{Y}) \approx \chi^2(\boldsymbol{Y}_0) + \frac{1}{2}\sum_{m,n}\frac{\partial \chi^2}{\partial Y_n \partial Y_m}y_n y_m \equiv \chi^2(\boldsymbol{Y}_0) + \boldsymbol{y}^T \hat{\mathbf{H}} \boldsymbol{y} \tag{4}$$

where the column-vector $\boldsymbol{y} \equiv \boldsymbol{Y} - \boldsymbol{Y}_0$ is a small displacement and $\chi^2(\boldsymbol{Y}_0)$ is a minimum. Note that the correlations $\overline{y_m y_n} \equiv \sigma_{mn}^2 = (\hat{\mathbf{H}}^{-1})_{mn}$. Matrix $\hat{\mathbf{H}}$ and its inversion $\hat{\mathbf{H}}^{-1}$ have the same eigenvectors, but their corresponding eigenvalues are inverse of each other.

A linear transformation $\boldsymbol{Y}' \equiv \hat{\mathbf{V}}\boldsymbol{Y}$, where $\hat{\mathbf{V}}$ is the matrix whose columns are the eigenvectors of $\hat{\mathbf{H}}$ reduces eq 4 to a sum of squares

$$\chi^2 = \chi^2(\boldsymbol{Y}_0) + \sum_m \lambda_m y_m'^2 \tag{5}$$

where each λ_m is an eigenvalue of $\hat{\mathbf{H}}$. Because $\chi^2(\boldsymbol{Y}_0)$ is a minimum of χ^2, all λ_m are larger than zero. The variances of y_m' are $1/\lambda_m$.

We can now consider $\boldsymbol{s}'$ and $\boldsymbol{s}$, linear sensitivities of $\boldsymbol{Y}$ and $\boldsymbol{Y}'$ to an external force $\mathcal{F}$ defined by $\boldsymbol{s} \equiv \partial \boldsymbol{Y}/\partial \mathcal{F}$ and $\boldsymbol{s}' \equiv \partial \boldsymbol{Y}'/\partial \mathcal{F} = \hat{\mathbf{V}}\boldsymbol{s}$. Because parameters y_m' are uncorrelated with each other, one can estimate the change $\Delta \mathcal{F}$ using estimates for $\Delta \boldsymbol{Y}'$ the conventional weighted average formula as follows

$$\langle \Delta \mathcal{F} \rangle = \frac{\sum_m \langle \Delta \mathcal{F}_m \rangle \lambda_m s_m'^2}{\sum_m \lambda_m s_m'^2} = \frac{\sum_m \langle \Delta Y'_m \rangle \lambda_m s_m'^2}{\sum_m \lambda_m s_m'^2} \tag{6}$$

where $\langle \Delta \mathcal{F}_m \rangle = \langle \Delta Y'_m \rangle/s_m'$ and $\sigma_{\Delta \mathcal{F}_m}^2 = 1/(\lambda_m s_m'^2)$ are the estimates of the temperature and its variance obtained using Y'_m alone and the notation $\langle \Delta Y'_m \rangle$ is used to denote the expectation value of $\Delta Y'_m$ given the data. The variance of $\Delta \mathcal{F}$ reads

$$\sigma_{\Delta \mathcal{F}}^2 = \frac{1}{\sum_m \lambda_m s_m'^2} \tag{7}$$

A straightforward example is a case of two parameters. For simplicity of calculations, we will use $\tilde{Y}_1 \equiv Y_1/\sigma_{11}$ and $\tilde{s}_1 \equiv s_1/$

σ_{11} and similar for Y_2 and s_2. In such a case, $\tilde{\sigma}_{11}^2 = \tilde{\sigma}_{22}^2 = 1$ and $\tilde{\sigma}_{12}^2 = \tilde{\sigma}_{21}^2 \equiv \rho$. The eigenvalues and the corresponding eigenvectors of the correlation matrix are $1 \pm \rho$ and $\boldsymbol{v}_{1,2} = (1, \pm 1)^T/\sqrt{2}$ respectively. The corresponding values of $\lambda_{1,2} = 1/(1 \pm \rho)$. Thus, eq 7 becomes

$$\sigma_{\Delta \mathcal{F}}^2 = \frac{1}{\frac{1}{1+\rho}\frac{(\tilde{s}_1+\tilde{s}_2)^2}{2} + \frac{1}{1-\rho}\frac{(\tilde{s}_1-\tilde{s}_2)^2}{2}} = \frac{1-\rho^2}{\tilde{s}_1^2 + \tilde{s}_2^2 - 2\rho\tilde{s}_1\tilde{s}_2} \tag{8}$$

If Y_2 is independent of $\mathcal{F}$ ($\tilde{s}_2 = 0$), the variance $\sigma_{\Delta \mathcal{F}}^2 = (1 - \rho^2)/\tilde{s}_1^2$ is smaller than or equal to $1/\tilde{s}_1^2$, the variance obtained from the analysis of Y_1 alone. The equality holds only for uncorrelated Y_1 and Y_2 ($\rho = 0$). Generally, $\sigma_{\Delta \mathcal{F}}^2 \leq 1/(\tilde{s}_1^2 + \tilde{s}_2^2)$.

The same estimates for $\mathcal{F}$ can be obtained using a G-factor defined by

$$G \equiv \sum_{m=1}^{M} Y_m' \lambda_m s_m' \tag{9}$$

The thermal sensitivity of G is $s_G = \sum \lambda_m s_m'^2$. One can see that $\langle G \rangle/s_G$ equals the right-hand side of eq 6 and that $\sigma_G^2/s_G^2 = \sum \sigma_{mm}'^2 \lambda_m^2 s_m'^2/(\sum \lambda_m s_m'^2)^2$ equals the right-hand side of eq 7. G can be expressed directly as a linear combination of Y_m by combining eq 9, $\boldsymbol{Y}' = \hat{\mathbf{V}}\boldsymbol{Y}$ and $\boldsymbol{s}' = \hat{\mathbf{V}}\boldsymbol{s}$ as follows

$$G = \sum_{m=1}^{M} w_m Y_m \tag{10}$$

All w_m can be determined analytically (if correlations and sensitivities of Y_m are known) or experimentally. The temperature sensitivity of the G-factor is the corresponding linear combination of s_m, that is, $\partial G/\partial T = \sum w_m s_m$ and can be calculated using the sensitivities of all contributing Y_m. Experimentally, one measures a large number of spectra in a short time interval such that the temperature change is insignificant during the measurements, and hence, fluctuations of $\langle Y_m \rangle$ are not affected by the temperature variance. The values of w_m are the values minimizing $\sigma_{\Delta \mathcal{F}}^2$.

■ ASSOCIATED CONTENT

ⓢ Supporting Information

The Supporting Information is available free of charge on the ACS Publications website at DOI: 10.1021/acsphotonics.9b00468.

Scanning electron microscopy, experimental setup, power dependence of γ_{zpl}, λ_{zpl}, and A_{zpl}, laser spot-size measurement, laser heating confocal and wide-field, example of correlation in two-parametric sensing, and examples of G_3-sensing with SiV-centers (PDF)

■ AUTHOR INFORMATION

Corresponding Author

*E-mail: taras@physics.uq.edu.au.

ORCID ⓘ

Sumin Choi: 0000-0002-7333-7945

Notes

The authors declare no competing financial interest.

■ ACKNOWLEDGMENTS

■ REFERENCES

(1) Vojinović, V.; Cabral, J.; Fonseca, L. Real-time bioprocess monitoring: Part I: In situ sensors. *Sens. Actuators, B* **2006**, *114*, 1083−1091.

(2) Donner, J. S.; Thompson, S. A.; Kreuzer, M. P.; Baffou, G.; Quidant, R. Mapping intracellular temperature using green fluorescent protein. *Nano Lett.* **2012**, *12*, 2107−2111.

(3) Kucsko, G.; Maurer, P.; Yao, N. Y.; Kubo, M.; Noh, H.; Lo, P.; Park, H.; Lukin, M. D. Nanometre-scale thermometry in a living cell. *Nature* **2013**, *500*, 54.

(4) Yang, J.-M.; Yang, H.; Lin, L. Quantum dot nano thermometers reveal heterogeneous local thermogenesis in living cells. *ACS Nano* **2011**, *5*, 5067−5071.

(5) Löw, P.; Kim, B.; Takama, N.; Bergaud, C. High-Spatial-Resolution Surface Temperature Mapping Using Fluorescent Thermometry. *Small* **2008**, *4*, 908−914.

(6) Shang, L.; Stockmar, F.; Azadfar, N.; Nienhaus, G. U. Intracellular thermometry by using fluorescent gold nanoclusters. *Angew. Chem., Int. Ed.* **2013**, *52*, 11154−11157.

(7) Wong, F. H.; Banks, D. S.; Abu-Arish, A.; Fradin, C. A molecular thermometer based on fluorescent protein blinking. *J. Am. Chem. Soc.* **2007**, *129*, 10302−10303.

(8) Baffou, G.; Rigneault, H.; Marguet, D.; Jullien, L. A critique of methods for temperature imaging in single cells. *Nat. Methods* **2014**, *11*, 899.

(9) Kiyonaka, S.; Sakaguchi, R.; Itaru Hamachi, T. M.; Yoshizaki, T.; Mori, Y. Validating subcellular thermal changes revealed by flouorescent thermosensors. *Nat. Methods* **2015**, *12*, 801−812.

(10) Suzuki, M.; Zeeb, V.; Arai, S.; Oyama, K.; Ishiwata, S. The 10^5 gap issue between calculation and measurement in single-cell thermometry. *Nat. Methods* **2015**, *12*, 802−803.

(11) Baffou, G.; Rigneault, H.; Marguet, D.; Jullien, L.; Kiyonaka, S.; Suzuki, M.; et al. *Nat. Methods* **2015**, *12*, 803.

(12) Shi, L.; Dames, C.; Lukes, J. R.; Reddy, P.; Duda, J.; Cahill, D. G.; Lee, J.; Amy Marconnet, K. E. G.; Bahk, J.-H.; Shakouri, A.; Prasher, R. S.; Felts, J.; King, W. P.; Han, B.; Bischof, J. C. Evaluating broader impacts of nanoscale thermal transport research. *Nanoscale Microscale Thermophys. Eng.* **2015**, *19*, 127−165.

(13) Ziabari, A.; Torres, P.; Vermeersch, B.; Xuan, Y.; Cartoixa, X.; Bahk, A. T. J.-H.; Koh, Y. R.; Parsa, M.; Ye, P. D.; Alvarez, F. X.; Shakouri, A. Full-field thermal imaging of quasiballistic crosstalk reduction in nanoscale devices. *Nat. Commun.* **2018**, *9*, 255.

(14) Jaque, D.; Vetrone, F. Luminescence nanothermometry. *Nanoscale* **2012**, *4*, 4301−4326.

(15) Brites, C. D.; Lima, P. P.; Silva, N. J.; Millán, A.; Amaral, V. S.; Palacio, F.; Carlos, L. D. Thermometry at the nanoscale. *Nanoscale* **2012**, *4*, 4799−4829.

(16) Neumann, P.; Jakobi, I.; Dolde, F.; Burk, C.; Reuter, R.; Waldherr, G.; Honert, J.; Wolf, T.; Brunner, A.; Shim, J. H.; et al. High-precision nanoscale temperature sensing using single defects in diamond. *Nano Lett.* **2013**, *13*, 2738−2742.

(17) Sekiguchi, T.; Sotoma, S.; Harada, Y. Fluorescent nano-diamonds as a robust temperature sensor inside a single cell. *Biophysics and Physicobiology* **2018**, *15*, 229−234.

(18) Aharonovich, I.; Greentree, A. D.; Prawer, S. Diamond photonics. *Nat. Photonics* **2011**, *5*, 397.

(19) Zhu, Y.; Li, J.; Li, W.; Zhang, Y.; Yang, X.; Chen, N.; Sun, Y.; Zhao, Y.; Fan, C.; Huang, Q. The biocompatibility of nanodiamonds and their application in drug delivery systems. *Theranostics* **2012**, *2*, 302.

(20) Liu, Y.; Gu, Z.; Margrave, J. L.; Khabashesku, V. N. Functionalization of nanoscale diamond powder: fluoro-, alkyl-, amino-, and amino acid-nanodiamond derivatives. *Chem. Mater.* **2004**, *16*, 3924−3930.

(21) Plakhotnik, T.; Aman, H.; Chang, H.-C. All-optical single-nanoparticle ratiometric thermometry with a noise floor of 0.3 $kHz^{-1/2}$. *Nanotechnology* **2015**, *26*, 245501.

(22) Alkahtani, M.; Jiang, L.; Brick, R.; Hemmer, P.; Scully, M. Nanometer-scale luminescent thermometry in bovine embryos. *Opt. Lett.* **2017**, *42*, 4812−4815.

(23) Alkahtani, M. H.; Alghannam, F.; Jiang, L.; Rampersaud, A. A.; Brick, R.; Gomes, C. L.; Scully, M. O.; Hemmer, P. R. Fluorescent nanodiamonds for luminescent thermometry in the biological transparency window. *Opt. Lett.* **2018**, *43*, 3317−3320.

(24) Wang, N.; Liu, G.-Q.; Leong, W.-H.; Zeng, H.; Feng, X.; Li, S.-H.; Dolde, F.; Fedder, H.; Wrachtrup, J.; Cui, X.-D.; et al. Magnetic Criticality Enhanced Hybrid Nanodiamond Thermometer under Ambient Conditions. *Phys. Rev. X* **2018**, *8*, No. 011042.

(25) de la Hoz, A.; Diaz-Ortiz, A.; Moreno, A. Microwaves in organic synthesis. Thermal and non-thermal microwave effects. *Chem. Soc. Rev.* **2005**, *34*, 164−178.

(26) Nguyen, C. T.; Evans, R. E.; Sipahigil, A.; Bhaskar, M. K.; Sukachev, D. D.; Agafonov, V. N.; Davydov, V. A.; Kulikova, L. F.; Jelezko, F.; Lukin, M. D. All-optical nanoscale thermometry with silicon-vacancy centers in diamond. *Appl. Phys. Lett.* **2018**, *112*, 203102.

(27) Fan, J.-W.; Cojocaru, I.; Becker, J.; Fedotov, I. V.; Alkahtani, M. H. A.; Alajlan, A.; Blakley, S.; Rezaee, M.; Lyamkina, A.; Palyanov, Y. N.; et al. Germanium-Vacancy Color Center in Diamond as a Temperature Sensor. *ACS Photonics* **2018**, *5*, 765−770.

(28) Alkahtani, M.; Cojocaru, I.; Liu, X.; Herzig, T.; Meijer, J.; Küpper, J.; Lühmann, T.; Akimov, A. V.; Hemmer, P. R. Tin-vacancy in diamonds for luminescent thermometry. *Appl. Phys. Lett.* **2018**, *112*, 241902.

(29) Choi, S.; Leong, V.; Davydov, V. A.; Agafonov, V. N.; Cheong, M. W.; Kalashnikov, D. A.; Krivitsky, L. A. Varying temperature and silicon content in nanodiamond growth: effects on silicon-vacancy centres. *Sci. Rep.* **2018**, *8*, 3792.

(30) Donley, E. A.; Plakhotnik, T. Statistics for Single Molecule Spectroscopy Data. *Single Mol.* **2001**, *2*, 23−30.

(31) Dragounová, K.; Potucek, Z.; Potocky, S.; Bryknar, Z.; Kromka, A. Determination of temperature dependent parameters of zero-phonon line in photoluminescence spectrum of silicon-vacancy centre in CVD diamond thin films. *J. Electr. Eng.* **2017**, *68*, 74−78.

(32) Lagomarsino, S.; Gorelli, F.; Santoro, M.; Fabbri, N.; Hajeb, A.; Sciortino, S.; Palla, L.; Czelusniak, C.; Massi, M.; Taccetti, F.; et al. Robust luminescence of the silicon-vacancy center in diamond at high temperatures. *AIP Adv.* **2015**, *5*, 127117.

(33) Plakhotnik, T.; Chennu, A.; Zvyagin, A. V. Statistics of Single-Electron Signals in Electron-Multiplying Charge-Coupled Devices. *IEEE Trans. Electron Devices* **2006**, *53*, 618−622.

(34) Landau, L. D.; Lifshitz, E. *Statistical Physics*, 3rd ed.; Butterworth−Heinemann, 1980; Vol. 5.

(35) Davydov, V. A.; Rakhmanina, A.; Lyapin, S.; Ilichev, I.; Boldyrev, K. N.; Shiryaev, A.; Agafonov, V. Production of nano-and microdiamonds with Si-V and NV luminescent centers at high pressures in systems based on mixtures of hydrocarbon and fluorocarbon compounds. *JETP Lett.* **2014**, *99*, 585−589.